RESEARCH ARTICLE

NANO · MICRO small
www.small-journal.com

Highly Flexible and Superelastic Graphene Nanofibrous Aerogels for Intelligent Sign Language

Kai Pang, Jingyu Ma, Xian Song, Xiaoting Liu, Chengqi Zhang, Yue Gao, Kaiwen Li, Yingjun Liu, Yuxin Peng,* Zhen Xu,* and Chao Gao**

Highly flexible and superelastic aerogels at large deformation have become urgent mechanical demands in practical uses, but both properties are usually exclusive. Here a trans-scale porosity design is proposed in graphene nanofibrous aerogels (GNFAs) to break the trade-off between high flexibility and superelasticity. The resulting GNFAs can completely recover after 1000 fatigue cycles at 60% folding strain, and notably maintain excellent structural integrity after 10000 cycles at 90% compressive strain, outperforming most of the reported aerogels. The mechanical robustness is demonstrated to be derived from the trans-scale porous structure, which is composed of hyperbolic micropores and porous nanofibers to enable the large elastic deformation capability. It is further revealed that flexible and superelastic GNFAs exhibit high sensitivity and ultrastability as an electrical sensors to detect tension and flexion deformation. As proof, The GNFA sensor is implemented onto a human finger and achieves the intelligent recognition of sign language with high accuracy by multi-layer artificial neural network. This study proposes a highly flexible and elastic graphene aerogel for wearable human-machine interfaces in sensor technology.

1. Introduction

Ultralight aerogels are attractive for their fascinating characteristics of low density, high porosity, and large surface area, enabling wide applications in electronics, thermal insulation, energy catalysis, and acoustic absorption.[1–4] Since 1931,[5] thousands of aerogels have been fabricated by conventional sol-gel method with diversified material components, including carbon, ceramic, polymer, and metal.[6,7] However, those conventional aerogels with 1D granular structure are frustrated by the intrinsic brittleness owing to the weak particle-particle interactions,[2,8] making their practical applications lagging far behind the fundamental research.

The structural design has been devoted to overcome the brittleness and improve the flexibility and elasticity of aerogels. On the one hand, the 1D nanofibrous aerogels typically exhibited excellent flexibility because of the high aspect ratio and good structural continuity of movable nanofibers. Many efforts[2,8,9] improved the elasticity by physical intertwining or chemical crosslinking of nanofibers, but the elastic strain is still limited below 60%, especially in long-term fatigue cycles. This drawback can be attributed to the highly densified nanofibrous network, and these aerogels can only generate out-of-plane plastic torsion of nanofibers to resist loading but resulting in large plastic deformation, especially for high strain. On the other hand, the representative graphene aerogels,[10,11] assembled by 2D nanosheet, demonstrated superior elasticity up to 95% recoverable strain. However, these aerogels were difficult to achieve the flexibility and easily generated the structural damage under bending caused by large out-of-plane stretching deformation.[12] Till now, realizing both the high flexibility yet superelasticity of aerogels at large deformation still remains a great challenge.

Here we design the trans-scale porosity structure to realize the high flexibility and superelasticity simultaneously for graphene nanofibrous aerogel (GNFAs) by hydroplastic foaming (HPF) of eletrospuning graphene oxide films. We verify the trans-scale structure of GNFA span six orders of magnitude from millimetres to nanometres, divided into two aspect of porosity: hyperbolic microcells and porous nanofibers. This leads to the large bending flexibility and superior elasticity even at large deformation of 90% strain. The flexible and elastic GNFAs display the high gauge factor (≈30) as strain sensor and we successfully applied as artificial intelligent devices to express sign language by multi-layer artificial neural network, reaching the high accuracy of 99.23%,

K. Pang, J. Ma, X. Liu, C. Zhang, Y. Gao, K. Li, Y. Liu, Z. Xu, C. Gao
MOE Key Laboratory of Macromolecular Synthesis and Functionalization
Department of Polymer Science and Engineering
Key Laboratory of Adsorption and Separation Materials & Technologies of Zhejiang Province
Zhejiang University
38 Zheda Road, Hangzhou 310027, P. R. China
E-mail: yingjunliu@zju.edu.cn; zhenxu@zju.edu.cn; chaogao@zju.edu.cn

X. Song, Y. Peng
Department of Sports Science
Zhejiang University
Hangzhou 310058, P. R. China
E-mail: yxpeng@zju.edu.cn

Y. Liu, Z. Xu, C. Gao
Shanxi-Zheda Institute of Advanced Materials and Chemical Engineering
Taiyuan 030032, P. R. China

The ORCID identification number(s) for the author(s) of this article can be found under https://doi.org/10.1002/smll.202400415

DOI: 10.1002/smll.202400415

which opened up large potential opportunities toward more engineering applications in intelligent wearable electronics.

2. Result and Discussion

2.1. Fabrication of Trans-Scale GNFAs

Trans-scale porous GNFAs were prepared by electrospinning and HPF method[13,14] from hybrid graphene oxide (GO) solution. There were three steps in this process. First, we chose sodium polyacrylate (PAAS) and GO as precursor solution to achieve the electrospinning nanofibers. The high molecular weight of PAAS (M_w = 30000000) was adopted to regulate the rheological property and spinnability of GO solution by relieving the barrier effect of 2D GO sheets.[13] Second, the freestanding GO nanofiber mat was obtained after collecting randomly dispersed nanofibers. Finally, the mat was directly transformed into GO nanofibrous aerogel with porous nanofiber layers by HPF method. In this process, many bubbles were generated between the GO layers with growth and fusion stages (Figure S1, Supporting Information) to form the porous aerogel. The following thermal annealing treatment recovered the crystal structure of graphene and removed residual polymers to obtain GNFA. The D peak in Raman spectra (Figure S2a, Supporting Information) was obviously lower than the GO-PAAS NFA, indicating the crystal defects were partially removed after high-temperature treatment at 1600 °C and completely restored after 2800 °C treatment. The split 2D peak of GNFA-2800 °C further revealed the graphene was transformed into a high-crystallinity graphite structure. These results were solidified by the XRD data (Figure S2b, Supporting Information) with sharp crystalline peaks at 26.1 and 26.6° with interlayer space of 0.341 and 0.335 nm for GNFA-1600 and 2800 °C, respectively. The disappeared Na 1s peak in XPS and oxygen-containing characteristic peaks in FLIR spectra (Figure S3, Supporting Information) further proved the PAAS was removed after high-temperature treatment.

We verified the trans-scale structure of GNFA by high-resolution scanning electron microscopy (HR-SEM), spanning six orders of magnitude from millimetres to nanometres (**Figure 1b**). There were two level of porous structures resulted by the bubble growth during the HPF process: one was the continuously lapped hyperbolic pores by fibrous solid walls (≈10 µm thickness) with a size of 100–500 µm, the other was the internal pores of fibers with nano-scale graphene walls. Figure 1c displays the transformation from large-size GO nanofiber mat to highly porous GNFA with a length of ≈30 cm and thickness of ≈3 mm. We revealed such a large-scale GNFA maintained superior structural integrity after severe deformations, such as folding and multiple bending, similarly holding the remarkably mechanical elasticity and flexibility as conventional sponges.

2.2. Hierarchical Foaming and Structural Regulation of GNFAs

The foaming of nanofibrous GO mat was divided into macro- and micro-scale processes with bubble nucleation and growth stages, deciding the aerogel density and fiber diameter of GNFA, respectively. At the macroscale (**Figure 2a,c**), the pore size (D_p) of GNFA was tuned from 4 to 220 µm by HPF time (t), representing the positive relation of $D_p \sim t^{0.80}$. These results showed that the density (ρ) was decreased with t, resulting a wide ρ range from 2 to 44 mg cm^{-3}. The density of GNFA was well controllable by the HPF process, which conformed to a function of $\rho \sim t^{-0.47}$. We revealed the height change (H/H_0) of GNFA was increased from 1 to 60 and the nanofibrous wall thickness was decreased from 6.5 to 1.2 µm with extended t (Figures S4 and S6a, Supporting Information), which was consistent with the density change. Furthermore, the H/H_0 and D_p of GNFA were also influenced by the foaming agent (N_2H_4 solution) concentration, exhibiting the same tendency with first increasing rapidly and then decreasing (Figures S5 and S6b, Supporting Information). The increased trend was attributed to the more bubble nucleation sites with high N_2H_4 concentration, resulting the generation of large bubbles by Ostwald ripening growth.[15] However, the over-high N_2H_4 concentration caused the higher surface tension, which cannot sustain the hyperbolic porous structure during drying, generating the thick fibrous walls (Figure S6c, Supporting Information) and facilitating the decreased H/H_0 and D_p.

At microscale (Figure 2b; Figure S4, Supporting Information), the originally compact nanofiber in GNFA expanded obviously by bubbles, generating porous graphene nanofiber with ultra-thin wall thickness. The diameter of nanofiber (D) in GNFA was regulated from 1.5 to 3.1 µm by HPF time (t), obeying a relationship of $D \sim t^{0.13}$ (Figure 2d). As depicted in Figure S5 (Supporting Information), we found the higher N_2H_4 concentration resulted in the larger diameter of graphene nanofiber, which peaked at 50% (Figure S6d, Supporting Information). When the N_2H_4 concentration increased up to 80%, the nanofiber could not maintain the porous structure and collapsed to dense state. It was also mainly attributed to the solvent surface tension surpassing the bearing limit of graphene nanowall during drying, causing the structural collapse. The hierarchical foaming process not only generates macropores with hundreds of micrometers size but also achieves the porous nanofibers with micrometer pores and nanometer walls, providing a new trans-scale porous structure design for modulating mechanical properties of aerogels.

2.3. Mechanical Properties of GNFAs

We systematically studied the mechanical properties of GNFAs by bending and compression tests (**Figure 3**). All the mechanical tests were performed with GNFA after 1600 °C treatment (ρ = 1.69 mg cm^{-3}) due to the easily-slipped graphite structure in GNFA-2800 °C caused the plastic deformation behavior (Figure S7a, Supporting Information). The GNFA exhibited superior bending flexibility, which was over the half-folding state at 60% strain. It can always keep excellent fatigue stability with high recoverability for long-term bending cycles up to 1000, as shown in Figure 3a. We presented the plots of the compressive curves for GNFA at set strain maxima of 20, 40, 60, and 80% (Figure S7b, Supporting Information), revealing the classical two characteristic deformation regimes in open-cell foams: a Hookean linear elastic regime below 60% strain with a stable modulus and a densification regime over 60% with dramatically increased modulus and strength. GNFA was subjected to a cyclic compression test with 10000 loading-unloading fatigue

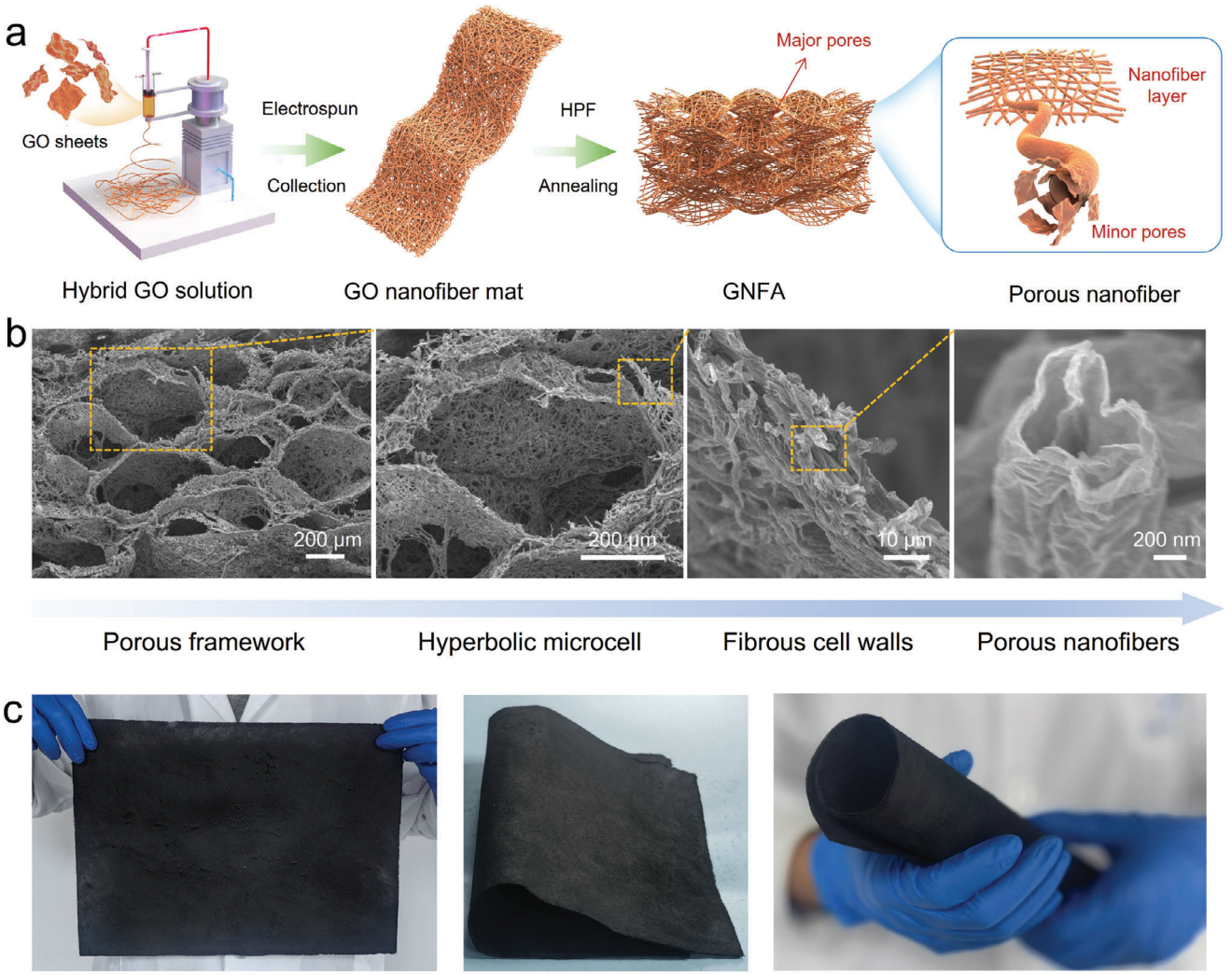

Figure 1. a) Schematic illustration for the preparation of GNFA. b) Trans-scale structure of GNFA by SEM images. c) The digital photos of a large-scale sample with folding and bending deformation.

cycles at a large of 90% (Figure 2b), and it exhibited slight plastic deformation (0.51% at 100th, 0.92% at 1000th, and 3.86% at 10000th), highlighting their structural robustness. Similarly, no significant decrease in the strength was observed for 10000 compression cycles, and NFGA retained over 75% of the maximum stress (Figure 2c). The energy loss coefficient was less than 0.4 and kept stable at compression, indicating less structural damage during fatigue tests. Besides, the GNFA exhibited the typical multiscale tensile fracture behaviors with elongation at a break of 11% and fracture strength of 2.1 kPa (Figure S7c, Supporting Information). Further dynamic compressive viscoelastic measurements revealed that the storage modulus (E') and loss modulus (E'') were nearly stable and independent of the temperature from −50 to 250 °C (Figure 2e), and E' was always higher than E''. A damping ratio of 0.1-0.35 over the entire range of temperature and frequency (Figure S8, Supporting Information) implied that the elastic response was predominant and carbon-based resilient GNFA exhibited excellent environmental adaptiveness.

In contrast to previously reported NFAs,[4,16–30] our GNFAs exhibited higher resilient strain and less mechanical loss during long-term fatigue cycles. As depicted in Figure 3e, we found the elastic strain limit of previous NFAs was below 60%, whereas, the GNFA realized the superior recoverability up to 90% even after 10000 fatigue cycles. Meanwhile, the stress remaining of GNFA still surpassed the majority of aerogels at different cycling tests (Figure 3f), confirming that our work has broken through the bottleneck of elastic nanofibrous aerogels. For previous nanofibrous aerogels, the fiber joints were easily slipped to release stress, especially under large deformation, resulting an elastic strain limit of 60%. To provide insight into the mechanism of elasticity, we performed in situ SEM observations under increasing compressive strain up to 90% (Figure 3g). The deformation of hyperbolic cells dominated in the whole compressive process without rotation or slippage of nanofibers. This proves that the loading force was released by the reversible deformation of macro- and micropores. The hyperbolic pores provided the recoverable energy by elastic buckling deformation of graphene fibrous walls. and the

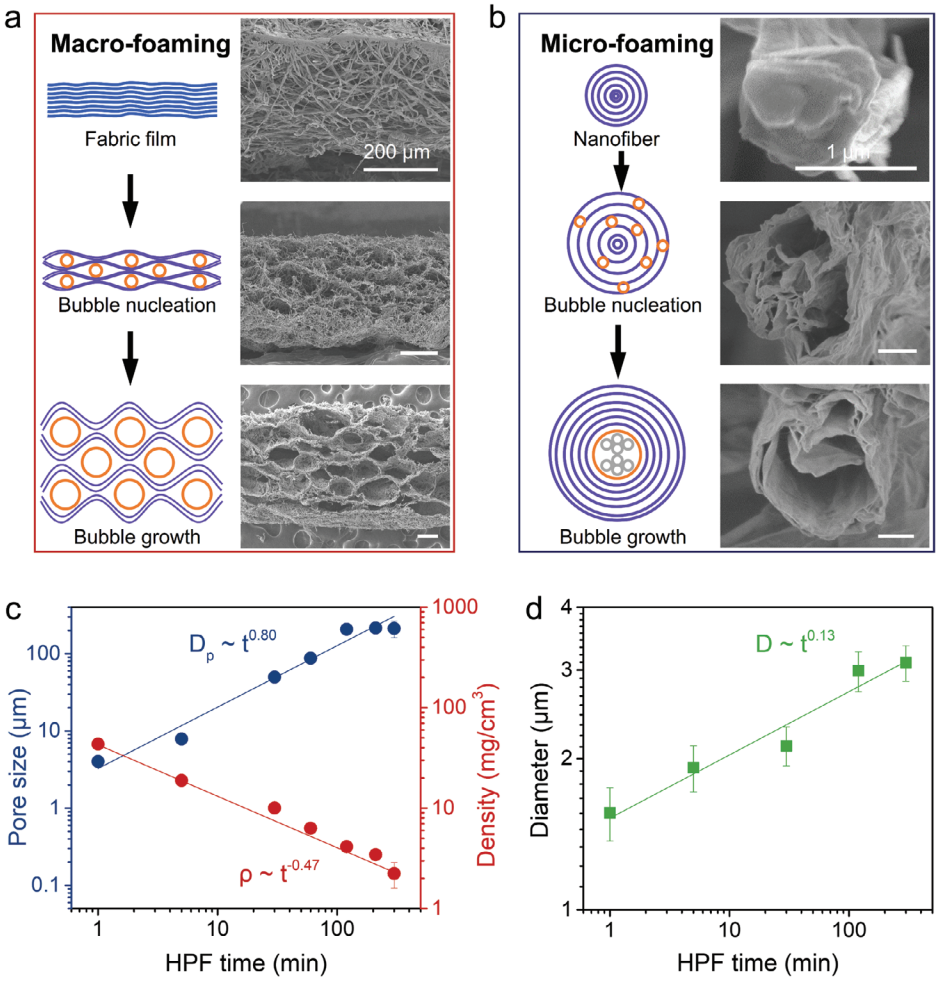

Figure 2. a) Illustration and structural evolution of macro-foaming between nanofibrous layers. b) Illustration and structural evolution of micro-foaming between fibers. c) The influences of HPF time on the pore size and density of GNFA. (c) The relationship between HPF time and nanofiber diameter.

internal pores in porous nanofiber ensured the enough free space for the elastic buckling of graphene walls, achieving the high elasticity at large deformation. Those results further demonstrated the mechanical superiority of our designed trans-scale porous structure in GNFAs. We have plotted the modulus and strength of a variety of GNFAs with a wide range of density from 1.6 to 49 mg•cm^{-3} during tensile and compressive processes (Figure S9, Supporting Information), indicating that the modulus (E) or strength (σ) scaled as $E/\sigma \sim \rho^{1.0}$. In contrast to this result, most previous aerogels exhibit a larger $E/\sigma \sim \rho$ scaling of >2.0 because of the inefficient stress transfer among structural units. Moreover, we revealed the electrical (σ_e) and thermal (λ) conductivities are also close to a scaling relation of $\sigma_e/\lambda \sim \rho^{1.0}$ (Figure S10, Supporting Information), testifying high-efficient connection in trans-scale GNFAs.

2.4. High-Sensitive Flexible GNFA Sensor for Human-Computer Interaction of Sign Language

The GNFAs were utilized as high-sensitive electrical sensors to detect the tension and flexion deformation. We assessed the sensor merits of a single GNFA sensor with two copper electrodes that were encapsulated by polydimethylsiloxane (PDMS) (**Figure** 4a). The graphene structure can be easily distinguished after infiltration (Figure S11, Supporting Information) without obvious structural damage. The curves of resistance change ($\triangle R/R_0$) with different densities were given in Figure 4b, and we found the lower density of GNFA with longer foaming time (Figure S12, Supporting Information) possessed the larger $\triangle R/R_0$ indicating higher sensitivity to strain (optimal density of 1.69 mg cm^{-3}). It can be attributed to the extremely high porosity of low-density GNFA, which provided the large free space for the deformation of hyperbolic graphene cell walls to achieve large sensor responses. The gauge factor (GF) of GNFA as a tensile sensor exhibits two linear regimes of 0–60% and 60–100% strain, and it can be up to 30 in the strain range of 60–100% and 7 below 60% strain (Figure 4c), surpassing most of carbon-based sensors.[31–34] We further revealed the gauge factor exhibited a tendency to increase (from 10 to 50%) and then decline (from 50 to 85%) with the increase of N_2H_4 concentration (Figure S12, Supporting Information). The increase trend mainly resulted by the larger average pores of GNFA at higher N_2H_4 concentration. But as mentioned, the over-high N_2H_4 concentration would

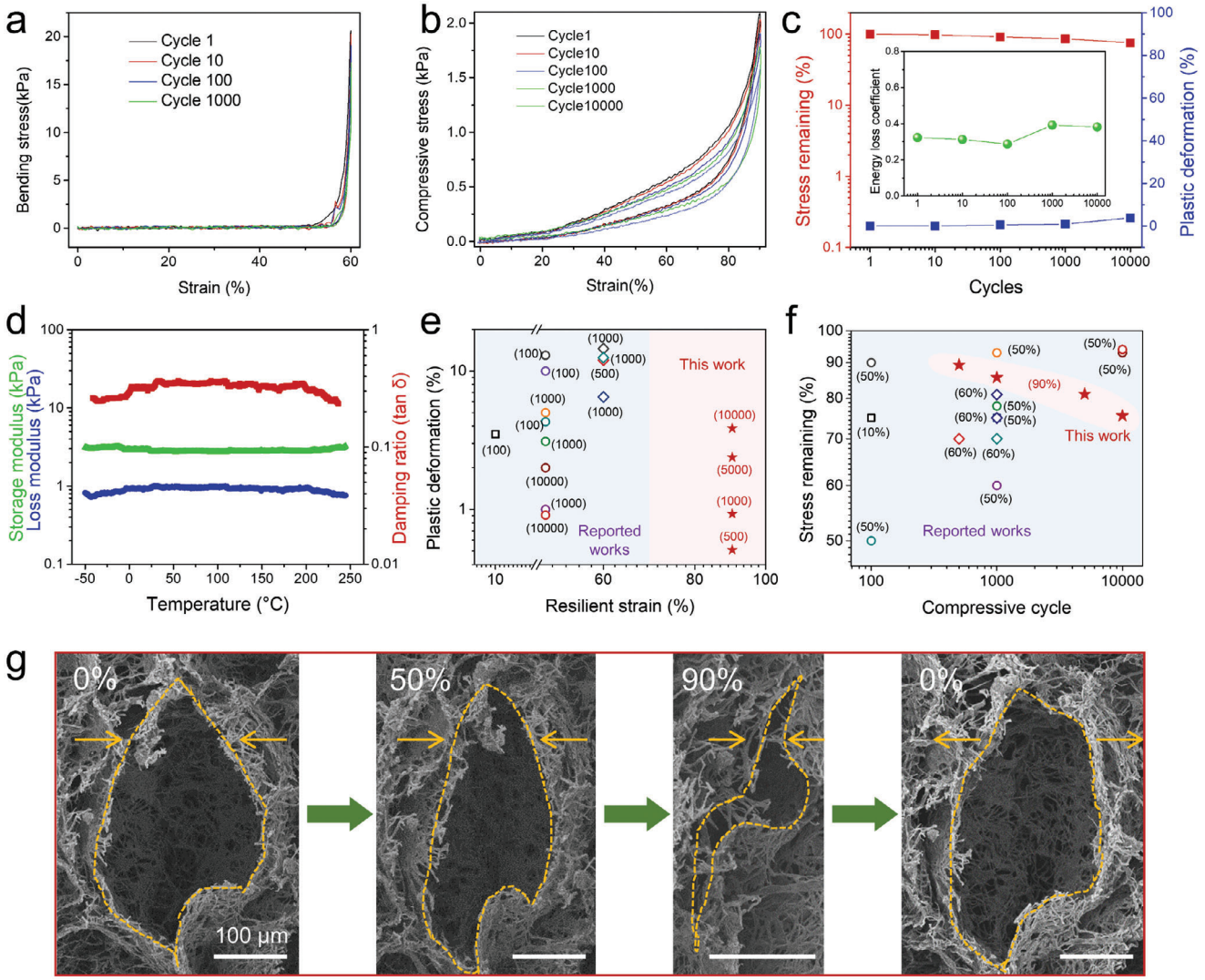

Figure 3. a) Bending strain-stress curves of GNFA during 1000 fatigue cycles. b) Compressive strain-stress curves of GNFA during 10 000 fatigue cycles. c) Stress remaining, plastic deformation, and energy loss coefficient versus compressive cycles. d) Storage modulus, loss modulus, and damping ratio of the CNFAs versus temperatures from −50 to 250 °C, with an oscillatory compressive strain of 3%. e) Plastic deformation versus resilient strain for nanofibrous aerogel materials. Numbers of compressive cycle are marked beside the corresponding dots in the chart. f) Stress remaining versus compressive cycles for nanofibrous aerogel materials. Compressive strains are marked beside the corresponding dots in the chart. g) In situ SEM observation of GNFA at the maximum compressive strain of 90%.

cause the shrinkage of hyperbolic porous structure, causing the reduction of gauge factor over 50% N_2H_4 concentration. As comparison, the GNFA sensor exhibited the higher strain sensitivity (gauge factor) in the wide strain range (Table S1, Supporting Information), possessing the better cycling stability to ensure the sensor reliability in practical applications. As a flexion sensor, we demonstrated the GNFA exhibited the linear response curves at all densities, and the maximum angle sensitivity was up to 1.2 (Figure 4d). To evaluate the stability and reliability of GNFA sensor, we performed the cycling tests to collect the force and voltage signals, respectively (Figure 4e–h). Whether tensile for 10 000 cycles or bending for 1000 cycles, the mechanical and sensing curves of the GNFA sensor only had small fluctuation, which can be used for reliable data processing in practical applications.

We equipped the 10 GNFA sensors onto human fingers and evaluated the sensing ability to achieve the human-computer interaction of sign language,[35] aided by multi-layer artificial neural network.[36–38] The wireless data acquisition (DAQ) was adopted to realize the real-time data collection (**Figure 5**a), which can obtain 10 different sensing curves for hand movement, such as the sign language of "A" and its corresponding curves in Figure 5b. To extend the universality, we acquired the 25 groups of electrical signals of sign language from "B" to "Z" as illustrated in Figure 5c and Figure S12 (Supporting Information). The detailed identification of sign language is shown in Figure 5d. We designed a conditioning circuit to improve the signal quality, where the modified signals were then collected by a microcontroller and sent to the upper computer through Bluetooth transmission. The graphic interface on upper computer extracted 6

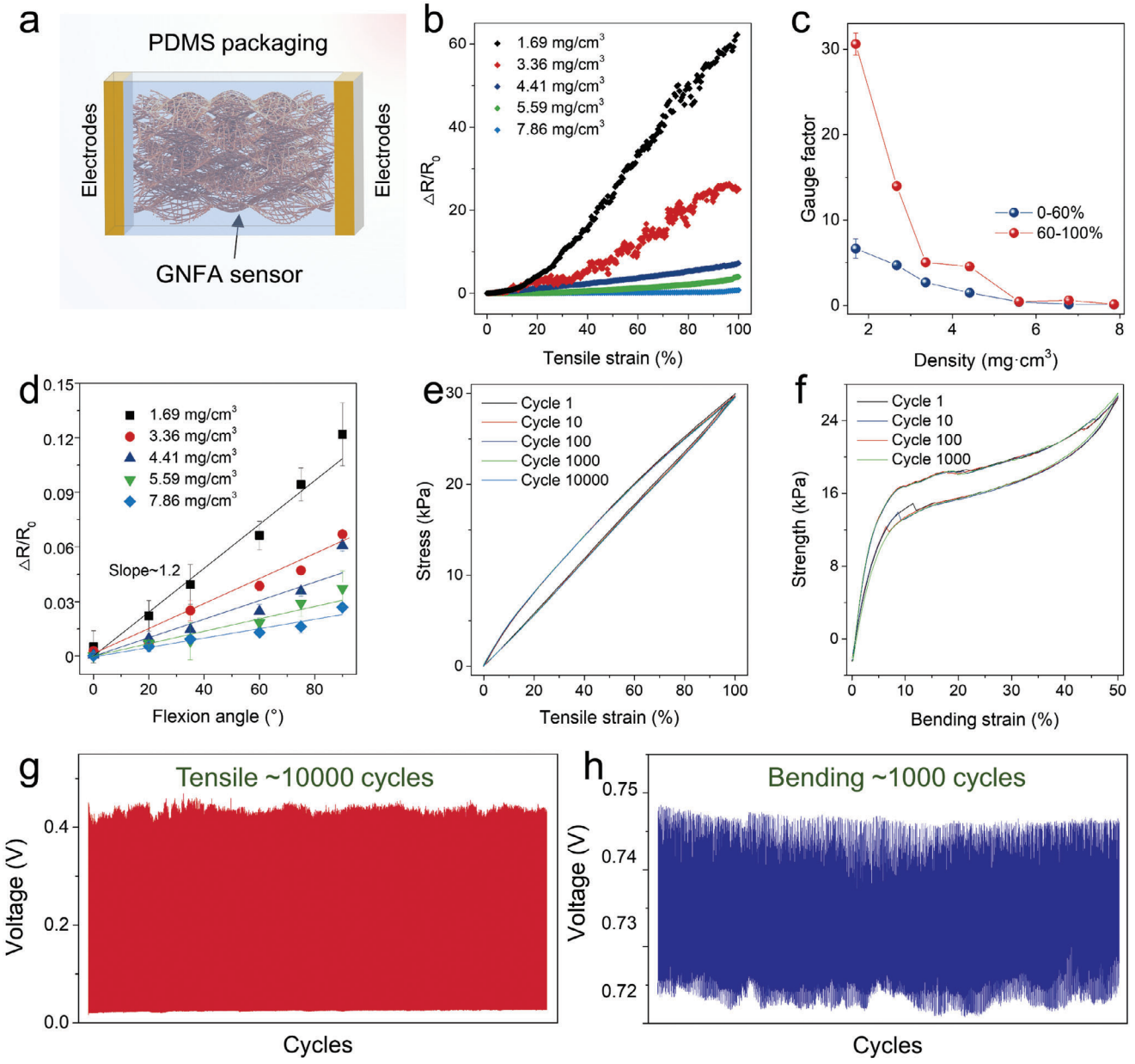

Figure 4. a) Structural diagram of flexible GNFA sensor. b) The resistance change ratio ($\triangle R/R_0$) of GNFA sensors with different density to 100% tensile strain. c) The gauge factor of GNFA sensors with different density. d) The $\triangle R/R_0$ of GNFA sensor with different density to flexion angle of 90°. Mechanical e) tensile (1000 cycles) and f) bending (10 000 cycles) performances of GNFA sensor during fatigue tests. Fatigue resistance of the GNFA sensor up to g) 100% tensile strain for 10 000 cycles and h) 50% bending strain for 1000 cycles.

features for all 10 channels to prepare the input set, namely Means, maximum value (Max), Entropy, root mean square (RMS), and variance (Var). The extracted feature sets were then processed by a pre-trained multi-layer Artificial Neural Network (ANN), benefiting from the remarkable ability to learn from complex data, which reached the high accuracy rate of 99.23% (Figure S13, Supporting Information). Figure 5e and Movie S1 (Supporting Information) given the real-time interaction between human hand and computer, and the sign language of "A" was rapidly mapped on the software interface by wireless transport. We think the application demo of high-sensitive GNFA sensors has great potential to promote the communication of speech disabled people.

3. Conclusion

A trans-scale porosity design was proposed to fabricate highly flexible and superelastic graphene nanofibrous aerogels by the combination of electrospun and hydroplastic foaming methods. The hyperbolic microcell with porous graphene nanofibers provided the high elastic recoverability at large deformation, enabling the good structural stability of trans-scale aerogels even at

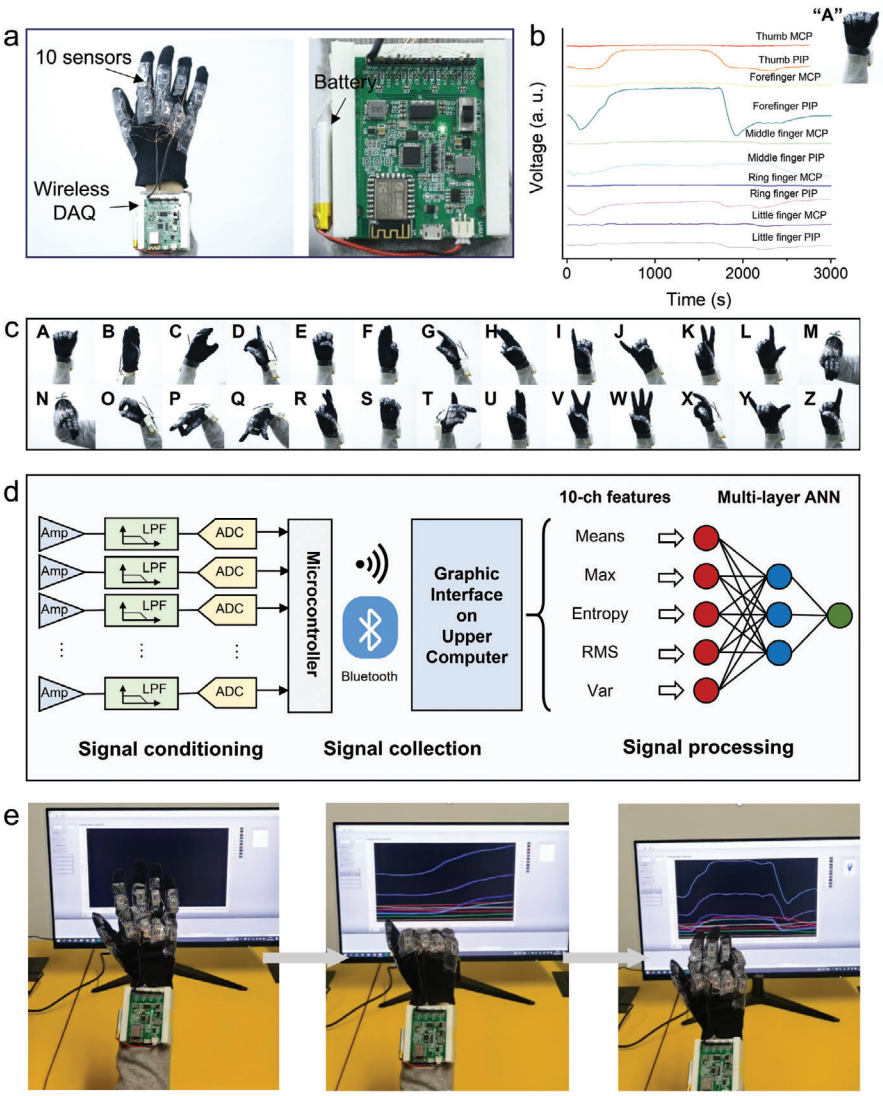

Figure 5. a) A human hand with 10 GNFA sensors and wireless DAQ (left). The structures of DAQ for collecting electrical signals (right). b) Collected signals of 10-channel sensors when making the sign language of "A". c) The 26 letters of sign language from A to Z. d) Flowchart of human-computer interaction of sign language, including signal conditioning, collection, and processing. e) The digital photos during testing procedure to identify the sign language of "A".

90% compressive strain and 10 000 fatigue cycles. The superior mechanical performance of graphene nanofibrous aerogels facilitated the fabrication of ultra-stable and reliable electrical sensors with high sensitivity. Furthermore, the precise human-computer interaction of sign language was realized by integrating with an artificial neural network, which can be rapidly recognize the 26 letters in real time. The greatly enhanced mechanical elasticity increases the practical worth of flexible nanofibrous aerogels for broad engineering applications in smart electronics, thermal insulation, catalysis, and acoustic absorption.

4. Experimental Section

Preparation of GO Nanofiber Mats: Aqueous GO solution (2 wt%) with an average lateral size of 10–20 µm was purchased from Hangzhou Gaoxi Technology Co. Ltd. (www.gaoxitech.com). Sodium polyacrylate (PAAS) (M_w = 30 000 000) was purchased from Shanghai Yuanye Bio-Technology Co. Ltd. Typically, 2.0 g PAAS powder was dissolved into 98 ml deionized water under vigorous stirring for 24 h. Then the solution was mixed with 100 ml aqueous GO solution under vigorous stirring for 1 h to obtain the electrospinning dope. The electrospinning process was performed on a single spinneret FT-1 spinning machine (Beijing Ucalery Industry Oriental Technology Co., Ltd.), and a piece of aluminum was covered on a metallic substrate as a collector. The feeding rate was controlled as 2 mL h^{-1} and the voltage added on the spinneret was 30 kV. The temperature and relative humidity were controlled at 60 °C and 15%, respectively. The distance between the spinneret and the collector was 15 cm. The obtained GO nanofiber mats were further used as the foaming precursor of the GNFAs.

Preparation of GNFAs: The GO nanofiber mat was soaked into N_2H_4 aqueous solution with varied concentrations (10-80 wt%) for different times (10–240 min) to realize hydroplastic foaming GNFAs. The GNFAs density can be tuned by changing the foaming time and N_2H_4 solution concentration according to the growth of produced bubbles. The following chemical reduction and high-temperature treatment (1600 °C for 2 h)

were conducted to obtain reduced hyperbolic graphene aerogels (HGAs). The mixed HI/HAc solution (volume ratio of 1:1) was used as a reduced reagent at 90 °C for 12 h. The thermal annealing process was conducted at argon atmosphere with a heating rate of 5 °C from room temperature to 1600 °C.

Fabrication of GNFA Sensors: GNFA sensors were prepared by adopting a vacuum impregnation method. The GNFAs were further annealed in 2800 °C treatment for 2 h with a heating rate of 10 °C from 1600 to 2800 °Cat argon atmosphere, to improve the electrical conductivity (Figure S10a, Supporting Information) and ensure the excellent sensing ability. The GNFAs were stuck to two pieces of copper foils (electrodes) by silver paste. The PDMS precursor with 10 wt% diluter (Dow Corning, pmx-200) was used as the infiltration agent of the GNFAs. Typically, the GNFAs were placed in a PTFE dish and immersed in the PDMS precursor with a metal mesh on top. Then the dish was transferred into a vacuum oven followed by degassing for 10 min to infiltrate the GNFAs with PDMS precursor. Finally, the filled GNFAs were cured in a 60 °C oven for 30 min. The graphene content depends on the densities of the GNFAs.

Details of Artificial Neural Networks: The ANN consists of a three-layer structure, containing an input layer, a single hidden layer, and an output layer. This configuration was chosen to balance the ability of the network to capture complex patterns in the data and the computational cost of training the model. This configuration was chosen to balance the ability of the network to capture complex patterns in the data and the computational cost of training the model. The weights connecting the nodes of the network were initialized randomly to conduct a startup for the system, and they were optimized by Adam. It commonly employs the cross-entropy as the loss function for classification tasks to quantify this discrepancy. The model was established by Tensorflow and accelerated by CUDA. The computational setup for training the ANN comprises an NVIDIA RTX 3060 GPU and an Intel i7 CPU. These tools provide a robust environment for defining the network, implementing the loss function and back-propagation algorithm, and executing efficient computations on the GPU.

Characterizations: The morphology and microstructure of GNFAs were characterized by field-emission SEM (Hitachi S4800) and TEM (FEI Titan G2 60–300). The compressive, bending, and tensile test was performed on an Instron Legend 2344 machine at a strain rate of 1 mm min^{-1}. The dynamic mechanical analysis was performed with DMA with environmental control (TAQ800). The GNFA sample was cut into a specific shape (1*1 cm) and put it between two plates. The test temperature from −50 to 250 °C was conducted with oscillatory compressive strain of 3% and a frequency of 2 Hz. The electrical properties of GNFAs were measured by the Keithley-2400 Source Meter using the four-wires method. The conductivity was calculated according to the equation $\sigma e = I/(R \times S)$, where I, S, and R were the length and the cross-sectional area and electrical resistance of the GNFAs, respectively. The cyclic performance of the GNFA sensors was evaluated by measuring the resistance change under the cyclic tensile test. The thermal conductivity was measured by laser thermal conductivity testing instrument (NETZSCH LFA467).

Supporting Information

Supporting Information is available from the Wiley Online Library or from the author.

Acknowledgements

K.P., J.M., and X.S. contributed equally to this work. This work is funded by the National Natural Science Foundation of China (52122301, 51973191, 52090030, and 52272046), the National Key R&D Program of China (2022YFA1205300), the Natural Science Foundation of Zhejiang Province (LR23E020003), the Pioneer and Leading Goose R&D Program of Zhejiang (2023C01190), the Fundamental Research Funds for the Central Universities (2021FZZX001-17), the China Postdoctoral Science Foundation (2021M702788), the International Research Center for X Polymers and Shanxi-Zheda Institute of New Materials and Chemical Engineering (2022SZ-TD012, 2022SZ-TD011, and 2021SZ-FR004).

Conflict of Interest

The authors declare no conflict of interest.

Data Availability Statement

The data that support the findings of this study are available from the corresponding author upon reasonable request.

Keywords

elasticity, flexibility, nanofibrous aerogels, trans-scale porous structure

Received: March 14, 2024
Published online:

[1] M. Zhang, S. Fang, A. A. Zakhidov, S. B. Lee, A. E. Aliev, C. D. Williams, K. R. Atkinson, R. H. Baughman, *Science* **2005**, *309*, 1215.
[2] X. Xu, S. Fu, J. Guo, H. Li, Y. Huang, X. Duan, *Mater. Today* **2021**, *42*, 162.
[3] S. Bag, A. F. Gaudette, M. E. Bussell, M. G. Kanatzidis, *Nat. Chem.* **2009**, *1*, 217.
[4] C. Jia, L. Li, Y. Liu, B. Fang, H. Ding, *Nat. Commun.* **2020**, *11*, 3732.
[5] S. S. Kistler, *Nature* **1931**, *127*, 741.
[6] X. Jiang, R. Du, R. Hübner, Y. Hu, *Matter* **2021**, *4*, 54.
[7] M. A. Aegerter, N. Leventis, M. M. Koebel, *Aerogels handbook*, Springer, Berlin, Germany, **2011**.
[8] Y. T. Liu, B. Ding, *Sci. Bull.* **2023**, *68*, 753.
[9] C. Liu, S. Wang, N. Wang, J. Yu, Y. T. Liu, B. Ding, *Nano-Micro Lett.* **2022**, *14*, 194.
[10] L. Qiu, Z. He, D. Li, *Adv. Mater.* **2018**, *30*, 1704850.
[11] Q. Zhang, D. Lin, B. Deng, X. Xu, Q. Nian, S. Jin, K. D. Leedy, H. Li, G. J. Cheng, *Adv. Mater.* **2017**, *29*, 1605506.
[12] F. Pan, F. Zhang, Y. Chen, Z. Liu, X. Zheng, B. Liu, *Extreme Mech. Lett.* **2020**, *36*, 100658.
[13] Z. Han, J. Wang, S. Liu, Q. Zhang, Y. Liu, Y. Tan, S. Luo, F. Guo, J. Ma, P. Li, X. Ming, Z. X.u Cao, *Adv. Fiber Mater.* **2022**, *4*, 268.
[14] K. Pang, X. Song, Z. Xu, X. Liu, Y. Liu, L. Zhong, Y. Peng, J. Wang, J. Zhou, F. Meng, J. Wang, C. Gao, *Sci. Adv.* **2020**, *6*, eabd4045.
[15] S.-T. Lee, C. B. Park, *Foam Extrusion: Principles and Practice*, CRC Press, Boca Raton, Florida, US, **2014**.
[16] J. Guo, S. Fu, Y. Deng, X. Xu, S. Laima, D. Liu, P. Zhang, J. Zhou, H. Zhao, H. Yu, S. Dang, J. Zhang, Y. Zhao, H. Li, X. Duan, *Nature* **2022**, *606*, 909.
[17] Y. Si, X. Wang, L. Dou, J. Yu, B. Ding, *Sci. Adv.* **2018**, *4*, eaas8925.
[18] Y. Si, J. Yu, X. Tang, J. Ge, B. Ding, *Nat. Commun.* **2014**, *5*, 5802.
[19] H. Wang, X. Zhang, N. Wang, Y. Li, X. Feng, Y. Huang, C. Zhao, Z. Liu, M. Fang, G. Ou, H. Gao, X. Li, H. Wu, *Sci. Adv.* **2017**, *3*, e1603170.
[20] Y. Si, X. Wang, C. Yan, L. Yang, J. Yu, B. Ding, *Adv. Mater.* **2016**, *28*, 9512.
[21] Z. L. Yu, B. Qin, Z. Y. Ma, J. Huang, S. C. Li, H. Y. Zhao, H. Li, Y. B. Zhu, H. A. Wu, S. H. Yu, *Adv. Mater.* **2019**, *31*, 1900651.
[22] L. An, J. Wang, D. Petit, J. N. Armstrong, K. Hanson, J. Hamilton, M. Souza, D. Zhao, C. Li, Y. Liu, Y. Huang, Y. Hu, Z. Li, Z. Shao, A. O. Desjarlais, S. Ren, *Nano Lett.* **2020**, *20*, 3828.
[23] L. Su, H. Wang, M. Niu, X. Fan, M. Ma, Z. Shi, S. W. Guo, *ACS Nano* **2018**, *12*, 3103.
[24] F. Wang, L. Dou, J. Dai, Y. Li, L. Huang, Y. Si, J. Yu, B. Ding, *Angew. Chem., Int. Ed.* **2020**, *132*, 8362.
[25] X. Zhang, X. Cheng, Y. Si, J. Yu, B. Ding, *ACS Nano* **2022**, *16*, 5487.
[26] L. Dou, X. Zhang, H. Shan, X. Cheng, Y. Si, J. Yu, B. Ding, *Adv. Funct. Mater.* **2020**, *30*, 2005928.

[27] F. Wu, Y. Liu, Y. Si, J. Yu, B. Ding, *Nano Today* **2022**, *44*, 101455.
[28] P. Guo, L. Su, K. Peng, D. Lu, L. Xu, M. Li, H. Wang, *ACS Nano* **2022**, *16*, 6625.
[29] L. Li, C. Jia, Y. Liu, B. Fang, W. Zhu, X. Li, L. A. Schaefer, Z. Li, F. Zhang, X. Feng, N. Hussain, X. Xi, D. Wang, Y. H. Lin, X. Wei, H. Wui, *Mater. Today* **2022**, *54*, 72.
[30] L. Su, H. Wang, M. Niu, S. Dai, Z. Cai, B. Yang, H. Huyan, X. Pan, *Sci. Adv.* **2020**, *6*, eaay6689.
[31] S. Ryu, P. Lee, J. B. Chou, R. Xu, R. Zhao, A. J. Hart, S. G. Kim, *ACS Nano* **2015**, *9*, 5929.
[32] Y. Lee, S. Bae, H. Jang, S. Jang, S. E. Zhu, S. H. Sim, Y. I. Song, B. H. Hong, J. H. Ahn, *Nano Lett.* **2010**, *10*, 490.
[33] T. Yamada, Y. Hayamizu, Y. Yamamoto, Y. Yomogida, A. Izadi-Najafabadi, D. N. Futaba, K. Hata, *Nat. Nanotech.* **2011**, *6*, 296.
[34] Y. Wang, R. Yang, Z. Shi, L. Zhang, D. Shi, E. Wang, G. Zhang, *ACS Nano* **2011**, *5*, 3645.
[35] W. C. Stokoe, D. C. Casterline, C. G. Croneberg, *A dictionary of American sign language on linguistic principles*, Gallaudet College Press, Washington, D.C, **1976**.
[36] X. Liu, J. Sacks, M. Zhang, A. G. Richardson, T. H. Lucas, J. V. Spiegel, *IEEE T. Circuits-II* **2016**, *64*, 1257.
[37] C. Sun, T. Zhang, C. Xu, *ACM T. Intel. Syst. Tec.* **2015**, *6*, 1.
[38] D. E. Rumelhart, G. E. Hinton, R. J. Williams, *Nature* **1986**, *323*, 533.

